

Whole-examination AI estimation of fetal biometrics from 20-week ultrasound scans

Lorenzo Venturini^{*}, Samuel Budd^{*}, Alfonso Farruggia^{*}, Robert Wright^{*}, Jacqueline Matthew^{*}, Thomas G. Day^{*†}, Bernhard Kainz^{*‡}, Reza Razavi^{*†}, Jo V. Hajnal^{*}

^{*}Department of Imaging Sciences, Faculty of Life Sciences and Medicine, King’s College London

[†]Guy’s and St Thomas’ NHS Foundation Trust, London

[‡]Department of Computing, Faculty of Engineering, Imperial College London, London

Abstract—The current approach to fetal anomaly screening is based on biometric measurements derived from individually selected ultrasound images. In this paper, we introduce a paradigm shift that attains human-level performance in biometric measurement by aggregating automatically extracted biometrics from every frame across an entire scan, with no need for operator intervention. We use a convolutional neural network to classify each frame of an ultrasound video recording. We then measure fetal biometrics in every frame where appropriate anatomy is visible. We use a Bayesian method to estimate the true value of each biometric from a large number of measurements and probabilistically reject outliers. We performed a retrospective experiment on 1457 recordings (comprising 48 million frames) of 20-week ultrasound scans, estimated fetal biometrics in those scans and compared our estimates to the measurements sonographers took during the scan. Our method achieves human-level performance in estimating fetal biometrics and estimates well-calibrated credible intervals in which the true biometric value is expected to lie.

Index Terms—Ultrasound; Fetal imaging; Machine learning; Bayesian estimation; Biometric measurement

I. INTRODUCTION

Ultrasound (US) imaging is routinely used in many countries during pregnancy to screen for fetal abnormalities, often at ~18-22 weeks [1]. Procedures typically involve imaging of standard planes of fetal anatomy and measurement of several fetal biometrics. In the UK, requirements for screening examinations are published in the Fetal Anatomy Screening Programme (FASP) standard [2].

Fetal biometrics are conventionally measured in single images: the operator pauses the US image stream on a specified view, then manipulates calipers to measure the anatomy. Some guidelines recommend that this whole procedure is repeated up to three times to ensure reliability [3]. Traditionally, these measurements have been done manually. Manual measurement of fetal biometrics displays significant expected-value bias [4]. Selection bias may also influence the planes used for measurement. Furthermore, these manual processes display significant inter-observer variability, ranging from 4.9% to 11.1% depending on the measurement [5].

Recent research has proposed methods for automating the detection of standard anatomical planes in during live scanning live scanning [6, 7, 8] and biometric measurements [9]. US machine manufacturers are increasingly integrating these tools in their equipment [10]. However, fetal biometry generally

still follows existing workflows that rely on operator selection of individual images. This does not take full advantage of the real-time nature of US, where a video stream of tens of frames per second is acquired. A fully automatic system could perform plane classification on every frame of the US stream and biometric measurement using all available data.

Fully automation would reduce human selection bias from plane selection and expected-value bias during measurement, potentially improving veracity, reproducibility and reducing operator dependence. Automating some key operator tasks could also reduce cognitive load, allowing the sonographer to focus more on the patient and on identifying signs of anomalies.

Evaluating every frame in a fully automatic system generates a very large number of measurements. A key challenge in making such a system useful for clinical practice, therefore, is to generate a single estimate from the vast resulting amount of information. There has been some work in developing methods to calculate fetal biometry from a video feed. Plotka et al [11] propose a system to select the best standard planes to extract biometry, and Lee et al [12] average convolutional neural network (CNN) outputs across a scan to estimate gestational age. Matthew et al [13] have proposed a system to automatically classify every frame in a US scan and extract fetal biometrics, but an operator still needs to select appropriate frames to report biometrics.

No work has, to our knowledge, sought to obtain an expected value of the biometry and a credible interval by combining all frame measurements while acknowledging potential outliers. This would represent a substantial departure from current clinical practice, which is fully focused on a selection and measurement of single images.

A. Contributions

We propose a real-time system that can identify standard planes and estimate fetal biometrics achieving and reporting progressively reducing uncertainties. The system is designed to seamlessly link into clinical practice during 20-week US screening scanning. We build upon Sononet [6] for standard plane detection, and pair it with automatic biometric estimation per frame, aggregating these to generate a progressive global estimate using a Bayesian framework. When used during live scanning, this results in progressively more reliable central

estimates and credible intervals for each biometric. The proposed method has the potential to improve clinical practice by providing robust measurements free from expectation bias, while reducing cognitive load on the sonographer.

II. METHODS

A. Datasets

The data for this work is taken from the iFIND project on fetal US, which recruited mothers attending a routine 20-week anomaly screening clinic in London, UK. 10000 volunteers gave consent to have their full 20-week US examinations (gestational age 18-22 weeks) recorded¹. The examinations were conducted on identical US machines (GE Voluson E8) by 145 professional sonographers following FASP protocols between 2015 and 2020. The sonographer identified, labelled, and saved standard plane images and manually measured biometrics. To best reflect the screening population, all scans were included regardless of whether the scan was reported as normal or abnormal.

Although the same machines were used throughout this study, software updates during this period changed the video resolution and the interface presented by the machine. Recordings were split across three resolutions depending on the date on which they were acquired: 678×576 , 980×784 , and 1280×1024 .

Due to operator error, technical glitches, and patient withdrawal of consent, not all of these scans could be used in the dataset: 7309 video recordings of prenatal US scans were used for this study.

To maintain patient anonymity, personal information was removed from the scan recordings and each scan was labelled with a numerical iFIND ID, numbered sequentially. We created training/validation/test splits across the dataset assigned subjects using the trailing digit of their iFIND ID. Scans with an iFIND ID with a trailing digit between 0-5 were used to train our models, 6-7 were used for validation, and 8-9 were held aside for testing and not used during training of any of our models. The demographic characteristics of patients across these folds, none of which showed statistically significant differences, are shown in Table I.

1) *Validation dataset* : Some of our methods were also validated using a small number of paired scans from a smaller study [13]. 23 volunteers were recruited after their 20-week anomaly scan for a follow-up scan. These ranged in gestational age from 20⁺⁰ to 24⁺⁰ gestational weeks (median 23GW), and had all screened as normal at their anomaly scan. These subjects had paired scans (encompassing the FASP planes and biometrics) conducted by separate sonographers on the same day, using a Philips EpiQ 7 US machine. These scans were not used to train our models.

B. Data labelling

The iFIND dataset includes full recordings of examinations that were labelled during scanning with standard planes and biometrics according to the FASP standard as shown in Table

II (note there is an additional background class for all other planes). These labels are present in the recording and were extracted automatically. Typically, a sonographer freezes the video stream once she identifies a suitable standard plane. Text labels and biometric measurements are then overlaid on the frame, which is saved for the sonographer’s report. Example frames with these overlays are shown in Figure 1.



Figure 1. Example frames with annotations and calipers. Shown are (a) a Brain-TV image, with annotations for head circumference, biparietal diameter and posterior ventricle, (b) a femur image, with the femur length measured and annotated. These frames were acquired and saved by a sonographer.

1) *Extraction of standard planes*: To find labelled planes in the recorded examinations, we automatically detected any pauses and freezes in the recordings, then used OCR software² to extract any added text labels. The text labels, including biometric labels (such as the Brain-TV view in Figure 1a) was then associated with standard planes and manually checked for consistency.

In the experiments performed in this paper, we removed segments where the sonographer froze the frame and added annotations. We did this by finding frames where over 95% of pixels did not change relative to the previous frame. This eliminates the sonographer’s own annotations from the recordings we used to test our methods.

2) *Biometrics*: In the UK, the FASP standard mandates a minimum of 5 biometric measurements per scan [2]³. These are measured across a range of standard planes, as shown in Table III.

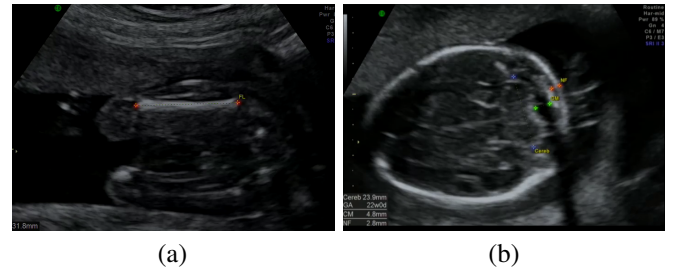


Figure 2. CaliperNet example heatmap outputs for (a) a femur image, and (b) a brain-CB image with labels for the cerebellum, cisterna magna and nuchal fold.

The calipers identifying a biometric are generally connected by a dotted line, with a text label next to them to identify

²For this project, we used the open-source Tesseract OCR package [14] to read text labels.

³Other biometrics, such as the nuchal fold (NF), must be measured in certain circumstances but are not required for every scan.

¹www.ifindproject.com

Data fold	Train	Validation	Test	lowest p-value
Total scans	4395	1457	1457	N/A
Abnormalities	528 (12.0%)	155 (10.6%)	163 (11.2%)	0.360
Live birth	4363 (99.2%)	1442 (98.9%)	1450 (99.5%)	0.375
Avg. GA	20w 3d	20w 3d	20w 3d	0.653
Nonwhite	1352 (30.8%)	458 (31.4%)	418 (28.7%)	0.166
Avg. BMI (kg / m ²)	24.7	24.9	24.9	0.448

Table I

PATIENT CHARACTERISTICS AND METADATA ACROSS THE DATA FOLDS USED FOR MODEL TRAINING. NONE OF THE PATIENT CHARACTERISTICS, INCLUDING GESTATIONAL AGE (GA), MATERNAL BODY MASS INDEX (BMI), OR PERCENTAGE OF ABNORMAL SCANS WERE SIGNIFICANTLY DIFFERENT ACROSS THE CHOSEN FOLDS.

Standard plane	Description
Head:	
Brain-CB	Transcerebellar view
Brain-TV	Transventricular view
Heart:	
3VT	3-vessel + trachea
LVOT	left ventricular outflow tract
RVOT	left ventricular outflow tract
4CH	4-chamber view
Other:	
Abdominal	
Femur	
Lips	
Kidneys	axial view
Profile	sagittal view
Spine-cor	coronal view
Spine-sag	sagittal view
Background	

Table II

LIST OF STANDARD PLANES RECOMMENDED UNDER FASP. WE ADDED A ‘BACKGROUND’ LABEL FOR FRAMES IN NONE OF THESE VIEWS.

the calipers (see Figure 2). To extract these biometrics, we trained a simple U-Net based neural network which we called CaliperNet (see Appendix A for details). We manually labelled 300 images of each biometric with the location of the calipers and trained a CNN to find calipers, with very good accuracy.

C. Pixel size estimation

The method described in Section III can find biometric endpoints on an image, but the measurements are given in pixels rather than millimetres. Moreover, pixel size can be changed during scanning by varying probe settings and machine zoom levels.

However, almost every frame shows a standard scale bar with prominent ticks at intervals $d_{\text{bar}} = 50\text{mm}$, with smaller ticks every 10mm and 5mm [15]. These ticks are at predictable positions on the screen: they can be seen clearly by looking at pixel values X_i along the correct scan line (see Figure 3).

Ticks can sometimes blend into bright structures shown on screen.

A simple, reliable and computationally efficient solution is to remove likely background signals from X_i by subtracting a 1D Gaussian filter, G_x , with standard deviation σ empirically selected to be 3px and keeping only positive values:

$$X'_i = \max(X_i - X_i * G_x(\sigma), 0), \quad (1)$$

We then computed the autocorrelation R_{XX} of the resulting filtered pixel values X'_i along the scan lines corresponding to the scale bar (see Figure 3):

$$R_{XX}(n) = \sum_i X'_i X'_{i+n}. \quad (2)$$

The first peak of the autocorrelation function corresponds to the spacing between axis ticks (in pixels). The size of individual pixels in millimetres L_x is given by

$$L_x = \frac{d_{\text{bar}}}{\max(R_{XX}(n))}. \quad (3)$$

To minimise quantisation noise, we estimate pixel size from the bars with the highest spacing.

D. Biometric measurement

To measure biometrics, we trained a the U-Net segmentation network using binary cross-entropy loss [9] to predict heatmaps constructed from the sonographer’s point annotations, extracted by CaliperNet, convolved with a Gaussian kernel. Figure 4 shows examples of training labels constructed this way. A separate CNN was trained for each standard plane, using the same U-Net architecture for each network and differing only in training planes and labels.

Biometrics were extracted from unseen images directly from the predicted heatmaps. For linear biometrics (FL and TCD), the Euclidean distance between the coordinates of the two highest maxima was used; For elliptical biometrics (HC and AC) we fit an ellipse to the heatmap using the least-squares criterion. The ellipse perimeter was then estimated using the formula recommended by the British Medical Ultrasound Society⁴ [16].

⁴The exact calculation of the perimeter of an ellipse is an infinite series. The cited guideline suggests using the first five terms of this series, which has a relative error of $< 0.01\%$ for most biologically plausible ellipse shapes.

Biometric		Type	No. of labels
Brain-TV:			
HC	Head circumference	Ellipse	8162
BPD	Biparietal diameter	Ellipse axis	8162
Brain-CB:			
TCD	Transcerebellar diameter	Linear	6906
Abdominal:			
AC	Abdominal circumference	Ellipse	6073
Femur:			
FL	Femur length	Linear	5718

Table III
BIOMETRICS MEASURED DURING THE 20-WEEK SCAN ACCORDING TO FASP GUIDELINES, AND THE NUMBER OF SUCH LABELS PRESENT IN THE IFIND1 DATASET.

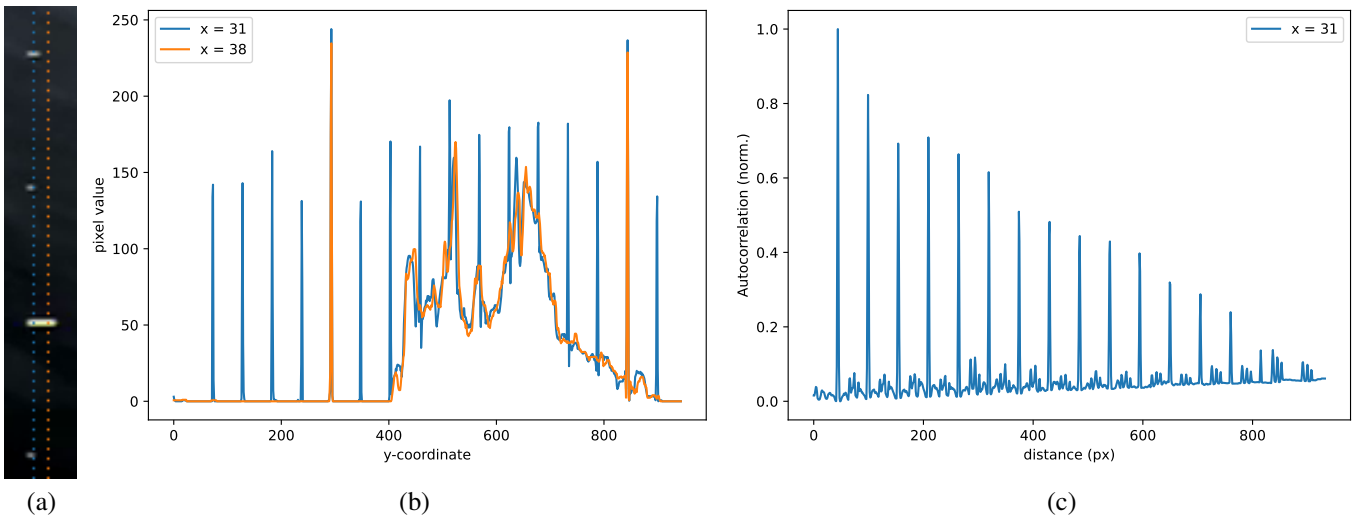


Figure 3. (a) Part of a scale bar, cropped from an image frame. Two lines are overlaid upon it. (b) The pixel values along those two scan lines for the entire frame. (c) The autocorrelation of the pixel values of the blue line after it has been processed with a high-pass filter.

Since BPD is mathematically equivalent to the minor axis of the ellipse used to segment the head, we calculated it directly from the head circumference label.

E. Whole-scan biometric estimation

In clinical practice, only a few frames are labelled by the sonographer. Generally, no more than three measurements are taken of each biometric [2] and the best subjective measurement is reported.

The automated methods described in Section II-D can extract measurements in all identified frames in which a given biometric is visible, resulting in hundreds or thousands of measurements per biometric. These form sample populations from which we wish to infer a true value and to estimate confidence intervals.

However, for each biometric there may be erroneous values, caused by misclassification of the target anatomical planes or by failure modes of the biometric CNN. Any estimation needs to reject or at least minimise the effect of these out-of-distribution measurements to reliably converge on the true biometric value.

Figure 5 shows our processing pipeline. Every frame from the US real time image stream is processed by Sononet to identify and label standard planes. Following Baumgartner et al [6], each frame is resized to a resolution of 288×224 and converted to greyscale.

Any frame identified with $> 95\%$ confidence as a standard plane with a FASP biometric is then processed by our CNNs to obtain a biometric measurement. The native frame is subsampled to a 384×288 resolution, with interface elements removed, and converted to greyscale and processed as described in Section II-D.

A quick check is then applied: if the proposed measurement is anatomically implausible (lower than the 3rd centile of the biometric at GA - 3 weeks or higher than the 97th centile at GA + 3 weeks), it is rejected. Furthermore, where the CNN's output does not allow an ellipse to be fitted or endpoints to be returned (for instance, where one distinct maximum is found, making it impossible to find two endpoints) the output is discarded.

These two filters (of plane-classification confidence and biometric measurements) may be undesirable for single-frame

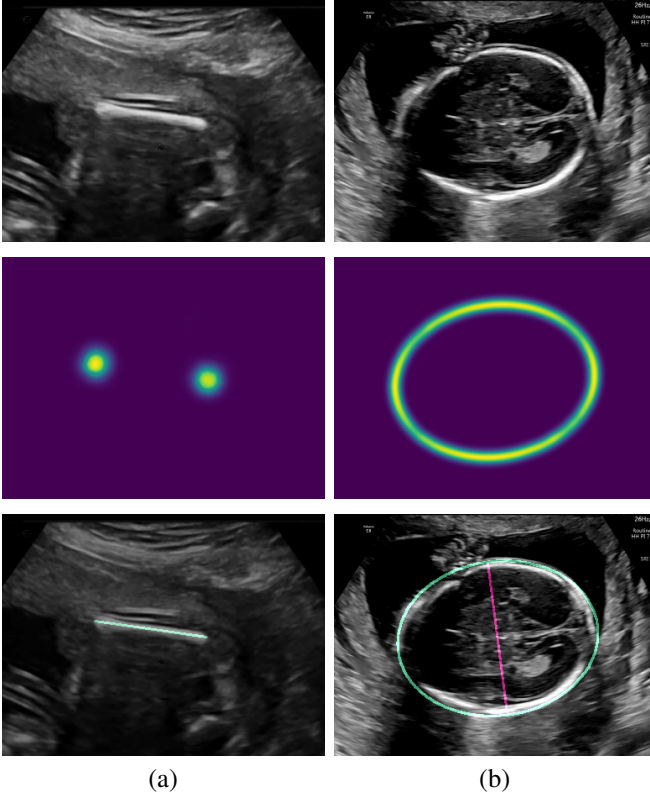


Figure 4. Images used for biometric training showing (a) femur, and (b) head views. The second row shows the training labels and the third row shows the CNN output overlaid on the image. For the head image, the HC output is shown in green and the BPD output in pink.

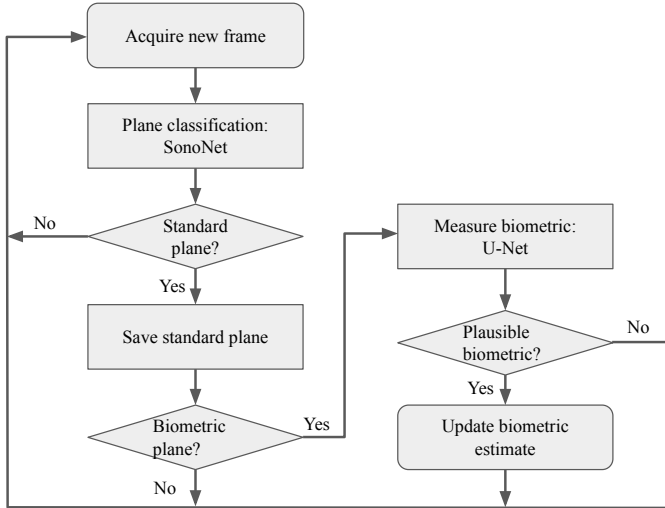


Figure 5. The pipeline which each frame in an US scan feed is processed by to estimate biometrics.

comparisons, as they discard some data. However, when estimating biometrics across a whole scan several hundred measurements of each biometric are often recorded: if some fraction of these are discarded, this only has a small impact on data availability. Appendix B details the proportion of biometric measurements discarded.

1) *Distribution of measurements*: This section describes how measurements of individual frames are aggregated and

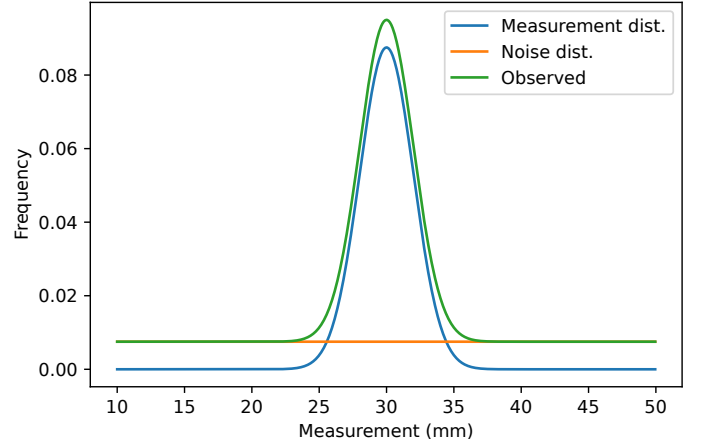


Figure 6. Idealised distribution of measurements for a biometric with true value 30mm. The observed distribution of measurements is a sum of a measurement distribution and a nuisance distribution of outliers.

outliers are rejected using a Bayesian framework.

Repeated measurements of the same biometric in different frames should cluster around a mean value. We modelled this using a normal distribution $\mathcal{N}(\mu, \sigma^2)$, with mean μ (if unbiased, this should be the true biometric value) and variance σ^2 (this depends on the precision of the biometric measurements).

Misclassified planes also return a biometric measurement and the biometric measurement process itself may fail even in a correctly identified plane. Since we have no information with which to model these failures we treat them as random and use a uniform distribution $U(a, b)$, over the full biological limits a and b , outside of which a measurement is rejected.

Thus, the observed distribution D_o of measurements will be a weighted sum of the measurement distribution $\mathcal{N}(\mu, \sigma^2)$ (for correct classifications) and a nuisance distribution $U(a, b)$ (for misclassifications). This can be represented by

$$D_o = P_t \mathcal{N}(\mu, \sigma^2) + (1 - P_t) U(a, b), \quad (4)$$

where P_t represents the proportion of valid measurements.

This equation contains several unknowns P_t, μ, σ^2 which can be estimated iteratively using a Bayesian approach, but each must be initialised.

2) *Estimating truth probability and distribution parameters*: To perform a Bayesian estimation, P_t needs to be initialised to a prior probability (in our approach, we set $P_{t_0} = 0.75$ for all biometrics, but it should converge on the true probability from any starting point other than 0 or 1), along with a prior weight W_0 ⁵. Prior estimates of the distribution parameters μ_0 and σ_0^2 need to be set, along with appropriate prior weights $W_{\mu,0}$ and $W_{\sigma^2,0}$.

For each new measurement x_i , we estimate the likelihood of it being a true measurement T or a nuisance sample \bar{T} using Bayes' rule:

$$P(T|x_i) = \frac{P(x_i|T)P_t}{P(x_i|\bar{T})(1 - P_t)} \quad (5)$$

⁵The estimate should converge on the true value of P_t regardless of what W_0 is set to, but setting it too high can cause it to converge slowly, while setting it too low can cause the estimate of P_t to oscillate inappropriately.

where $P(x_i|T)$ is the value of $\mathcal{N}(\mu, \sigma^2)$ at x_i , and $P(x_i|\bar{T})$ is the value of $U(a, b)$ at value x_i . This returns $P(T|x_i)$, the probability that this measurement was sampled from the true measurement distribution.

Finally, P_t and the distribution parameters μ, σ^2 can be updated for this biometric using a weighted cumulative average:

$$P_{t_i} = \frac{P(T|x_i) + W_{i-1}P_{t_{i-1}}}{W_{i-1} + 1} \quad (6)$$

$$\mu_i = \frac{x_i P(T|x_i) + W_{\mu, i-1} \mu_{i-1}}{P(T|x_i) + W_{\mu, i-1}} \quad (7)$$

$$\sigma_i^2 = \frac{(x_i - \mu_{i-1})^2 P(T|x_i) + W_{\sigma^2, i-1} \sigma_{i-1}^2}{P(T|x_i) + W_{\sigma^2, i-1}} \quad (8)$$

and their weighting factors can be updated using

$$W_i = W_{i-1} + 1 \quad (9)$$

$$W_{\mu, i} = W_{\mu, i-1} + P(T|x_i) \quad (10)$$

$$W_{\sigma^2, i} = W_{\sigma^2, i-1} + P(T|x_i). \quad (11)$$

As the noise distribution is taken to be uniform, there is no need to update estimates of its terms.

The estimates for μ and σ^2 are updated in real time and independently. At any given moment, the estimate of μ is the best estimate of the true value of the biometric of interest. Meanwhile, the estimate of σ^2 can be used to calculate the standard error $\hat{\sigma}_i$, of that estimate to find credible intervals for the biometric, given by

$$\hat{\sigma}_i = \frac{\sigma_i}{\sqrt{W_{\sigma^2, i}}}. \quad (12)$$

The 95% credible interval is given by the range $\mu_i \pm 2\hat{\sigma}_i$.

III. EXPERIMENTS

The variability in biometric measurements between two sonographers arises from two components: image selection for measurement and caliper placement within each image. Previous work has shown that 50-80% of variability between humans can be explained by caliper placement [5], leaving 20-50% of variability accounted for by image selection. The proposed whole-scan method eliminates this second source of noise by processing every frame in a scan with no manual intervention and seeks to reduce the effect of random error in caliper placement by aggregating measurements from many individual frames.

We performed three experiments to quantify the reliability of our biometric estimates:

- 1) Using our biometric CNNs to independently measure the same frames that sonographers labelled. This tests the biometric measurement performance of our CNNs and compares it to published estimates of inter-rater differences in caliper placement on a single image. Note this is still a restricted problem, requiring human intervention to perform frame selection. For these single-image experiments, biometrics were estimated automatically in the same frames that sonographers chose to make their manual annotations. We trained one CNN

per standard plane (from subjects in the training set) and tested it using the subjects in the test set using the unannotated copies previously extracted for all frames in the iFIND test set: 1516 in the brain-TV standard plane, 1360 for brain-CB, 1205 for abdominal, and 1124 for femur.

- 2) Aggregating biometric measurements across a whole recorded scan to obtain global estimates for the scan and comparing to sonographer manual measurements. This experiment considers a more unconstrained problem with no human interaction. It does not control for individual frame selection, so our results can be compared to inter-rater variability in biometric measurement from different scans. All 1457 recordings in the test set were used. The final estimate of each biometric, along with credible intervals, was reported.
- 3) Conducting a test-retest experiment on the paired scan data described in Section II-A1. Finally, we conducted a test-retest experiment on the paired scan data described in Section II-A1. We ran the full pipeline on paired scans of the same subject acquired on the same day using a different scanner from the training dataset. We then compared biometrics from each scan and measured test-retest variability of our algorithm. The scans here were performed on an US machine by a different manufacturer from the training data, which allowed us to examine domain shift.

All experiments were conducted on a single Nvidia GeForce RTX 3080 GPU.

A. Validation of distribution choice

Section II-E models the distribution of measurements of each biometric with a mixture of a uniform distribution and a Gaussian distribution

$$D = P_t \mathcal{N}(\mu, \sigma^2) + (1 - P_t) U(a, b). \quad (13)$$

This has three parameters P_t, μ and σ which are tuned iteratively to incoming data. This model assumes that incoming measurements follow a Gaussian distribution (if correctly classified) or a uniform distribution (if noise), which can be tested. We therefore examined the output biometric measurements to check the appropriateness of this model.

IV. RESULTS

A. Single-frame biometric estimation

A valid biometric estimate (following the constraints outlined in Section II-E) was obtained in approximately 90% of cases across all biometrics. Table IV shows performance on the unlabelled copies of the frames labelled by sonographers in the test dataset.

Using the sonographer measures as the reference point, the automated single frame performance showed bias of less than 1% and mean square difference (MSD) of less than 5% except for TCD which showed a MSD of just over 10%. Where inter-observer data is available for manual measurements, the automated approach could be seen to have an average of 41% lower agreement with the human rater.

Structure	Bias (mm)	MSD (mm)	Human MSD
HC	+0.11 mm (+0.07%)	4.34mm (2.68%)	2.70mm (1.8%)
BPD	+0.06mm (+0.17%)	1.28mm (3.20%)	N/A
AC	+1.51mm (+0.98%)	5.03mm (3.26%)	4.03mm (2.8%)
FL	0.00mm (0.00%)	1.53mm (4.67%)	1.02mm (2.9%)
TCD	-0.16mm (-0.75%)	2.1mm (10.1%)	N/A

Table IV

COMPARISON OF THE BIOMETRIC MEASUREMENTS OBTAINED ON THE TEST SET OF THE iFIND DATASET. ‘BIAS’ REFERS TO THE AVERAGE DIFFERENCE IN MEASUREMENT BETWEEN OUR METHOD AND HUMAN SONOGRAPHERS. ‘MSD’ IS THE MEAN-SQUARED DIFFERENCE BETWEEN PAIRS OF MEASUREMENTS. THE ‘HUMAN MSD’ COLUMN IS POPULATED WITH VALUES OF INTER-OBSERVER VARIABILITY REPORTED BY SARRIS ET AL [5].

Biometric	Bias	MSD	MAD (mm)	std. err (mm)	within human 95%
HC	-0.30mm (-0.18%)	3.23mm (1.99%)	2.50mm (1.42%)	3.39mm	94.7%
BPD	+0.90mm (+1.89%)	1.86mm (4.65%)	1.11mm (2.31%)	0.95mm	N/A
AC	-0.49mm (-0.31%)	5.55mm (3.60%)	4.23mm (2.74%)	3.26mm	96.6%
FL	-0.51mm (-1.59%)	1.63mm (4.99%)	1.19mm (3.64%)	1.12mm	93.9%
TCD	+0.27mm (+1.32%)	0.91mm (4.37%)	0.68mm (3.28%)	0.47mm	N/A

Table V

COMPARISON OF HUMAN MEASUREMENTS TO MACHINE ESTIMATES TAKEN ACROSS A WHOLE SCAN. ‘MAD’ REFERS TO MEAN ABSOLUTE DIFFERENCE BETWEEN HUMAN AND MACHINE MEASUREMENTS. THE ‘WITHIN HUMAN 95%’ COLUMN SHOWS THE PERCENTAGE OF BIOMETRICS IN THE TEST SET WHERE THE HUMAN-MACHINE DIFFERENCE IS WITHIN 95% OF HUMAN-HUMAN INTER-OBSERVER DIFFERENCES (TAKEN FROM (author?) [5])

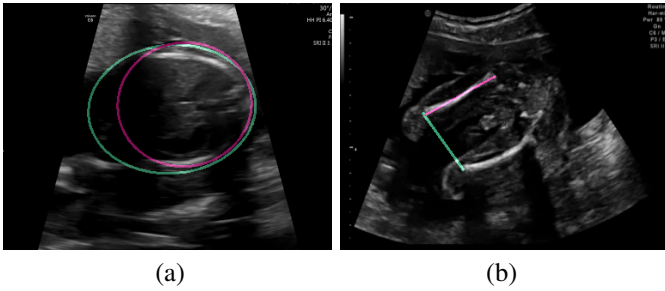


Figure 7. Two failure cases of biometric estimation in (a) HC, and (b) FL. The pink annotation shows the ground truth measurement made by a sonographer, while the green annotation is the automatic one made by our CNNs.

B. Whole-scan processing

Figure 8 shows how a biometric estimate (in this case HC) changes over time during one exemplar scan, overlaid with measurements from individual frames. Initially the prior dominates, estimating the 50th percentile for the age with wide error bars. As the number of frames contributing measurement values increases the overall estimate becomes more stable and resistant to outliers. Although individual frame measurements show significant noise, including extreme values (which are probabilistically discounted by our system), the credible interval progressively shrinks with increasing data. Figure 9 shows this happening in real time over 3 seconds of scanning.

Figure 10 shows Bland-Altman plots for human and machine measurement on the same subjects for three biometrics, with 95th percentile intervals overlaid for three biometrics. The difference between human measurements⁶ and machine estim-

⁶Human measurements were taken from sonographers’ reports after each scan.

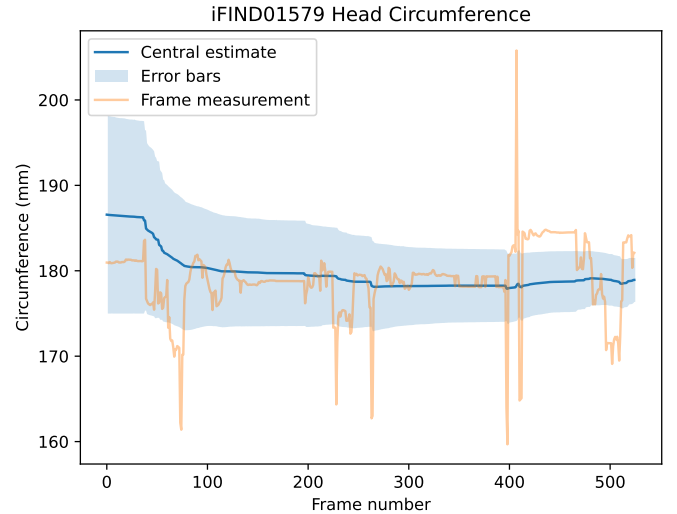


Figure 8. Evolution over time of the HC estimate in an individual subject, overlaid with credible intervals and individual frame measurements.

ates can be compared to inter-rater disagreement measured by Sarris et al [5]. Our 95th percentile intervals are overall very similar to human inter-rater variability for HC, AC, and FL. 95.1% of machine-human measurement differences (across these three biometrics) lie within the 95% range of human differences.

C. Paired scan data

We also conducted a test-retest experiment to measure reliability across repeated scans of the same subject.

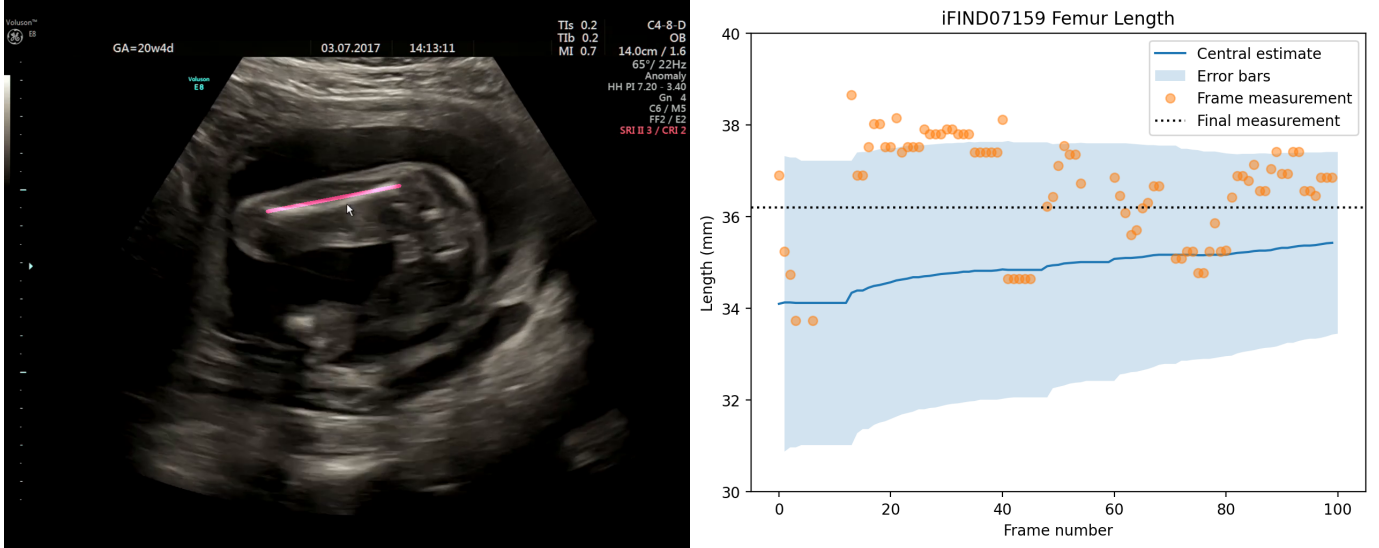


Figure 9. A still image from a video showing real-time measurement of biometrics and updating of the biometric estimate. In three seconds of real-time scanning, our system acquired 83 FL measurements and updated its FL estimate from 34mm (the prior, based on the average FL for this gestational age) to 36mm. The full video clip can be found at <http://www.ifindproject.com/wp-content/uploads/sites/79/2023/12/realtime.gif>

Biometric	MSD	Standard deviation	Human s.d. (full scan)	Number of pairs
HC	2.60mm (1.25%)	1.23%	2.75%	15
BPD	0.79mm (1.36%)	1.17%	N/A	15
AC	4.61mm (2.51%)	2.50%	5.05%	17
FL	0.97mm (2.44%)	2.44%	5.56%	10
TCD	0.57mm (2.33%)	1.62%	N/A	8

Table VI

TEST-RETEST RELIABILITY OF OUR MODEL OUTPUTS FROM PAIRED SCANS OF THE SAME SUBJECT. THE ‘HUMAN S.D.’ COLUMN IS POPULATED WITH RESULTS BY SARRIS ET AL [5].

Table VI shows the mean-square difference (MSD) and the standard deviation of the difference in the final biometric estimates from the test-retest experiment using data from 20 subjects scanned twice on the same day by different sonographers, as described in Section II-A1⁷. Not all pairs of scans had sufficient frames visible of each biometric in both scans: the number of pairs available for analysis is shown in the table.

D. Measurement distributions

Figure 11(a) shows the distribution of all femur length measurements across the test dataset. The values were demeaned and then aggregated across all scans.

Figure 11(b) shows the cumulative distribution function (cdf) of all measurements obtained that way, as well as the best-fit theoretical model distribution for this data. The global best-fit parameters for the femur length were $P_t = 0.79$, $\mu = 0$ and $\sigma = 1.8$ mm.

Similar curves were found for the other biometrics examined with comparable goodness of fit.

⁷We measured percent standard deviation in this table to ensure comparability with the measurements reported by Sarris et al [5], who reported human standard deviation. They examined a slightly different gestational age range, so we report percent standard deviation to normalise for that.

V. DISCUSSION

Our experiments show that the proposed workflow can improve the accuracy and repeatability of biometric estimation. In single frames, our models generally produce more variable biometric estimates than humans. However, when estimating biometrics across an entire examination, our estimates are in line with those made by sonographers (machine-human MSD \sim human-human MSD). Paired scan data also shows that our results are highly repeatable, with little difference across scans of the same subject. This latter test is a direct analogue of inter-rater testing by human observers and results were in closer agreement than for manual measurement.

A. Single-frame biometric estimation

Section IV-A compares our model’s performance in individual frames to that of a human. We generally find good agreement with sonographer measurements. Sarris et al [5] report inter-observer differences when two sonographers manually place calipers on the same US frame for three biometrics. When referenced to the corresponding human measurements, the machine measurements in this experiment across all biometrics show more divergence than humans do

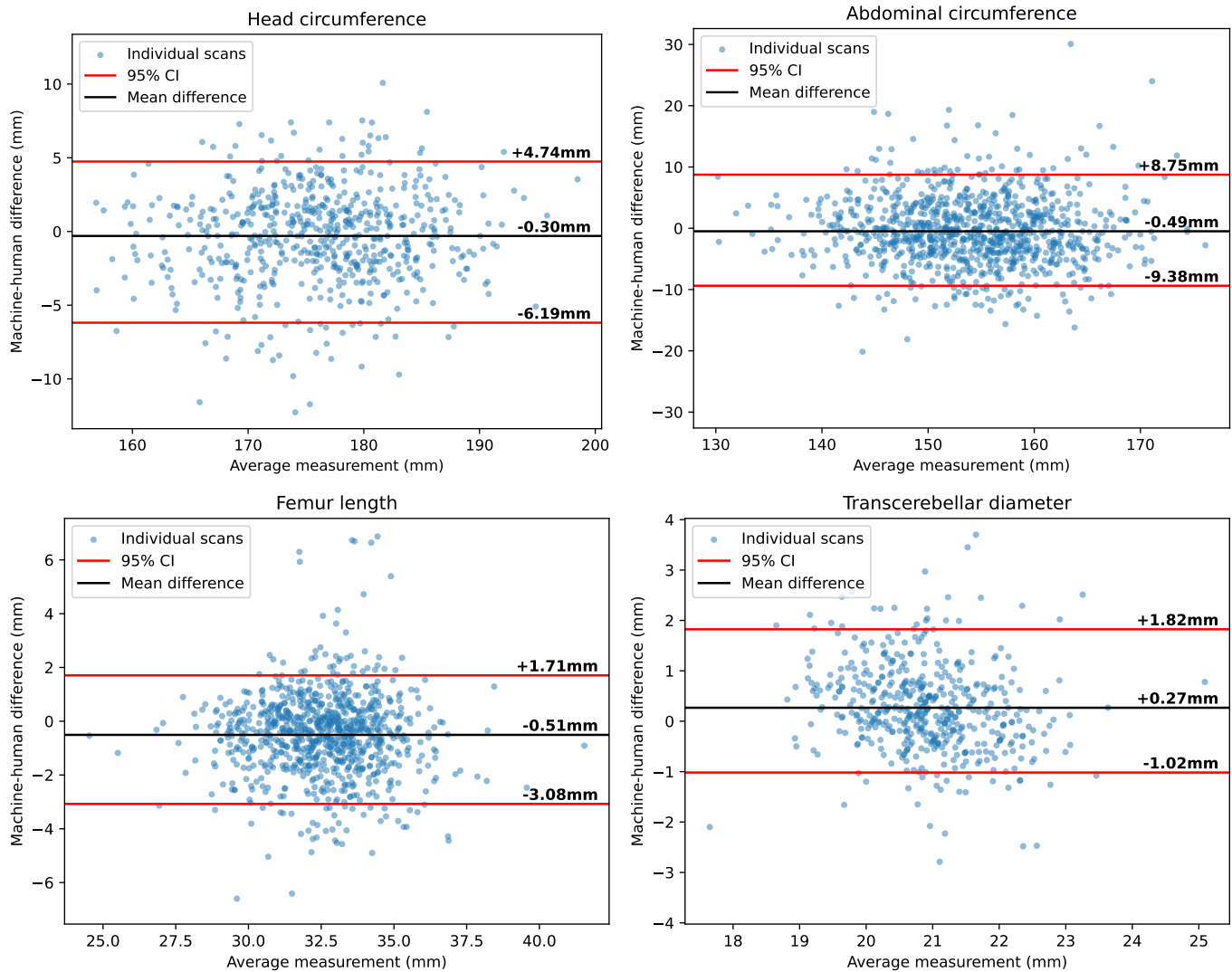


Figure 10. Bland-Altman plots showing the differences between the sonographer’s measurements and our own across all complete recordings in the test dataset.

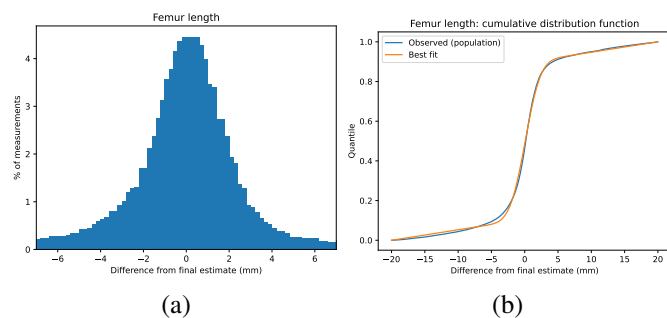


Figure 11. (a) The histogram of all femur length measurements made in individual frames in the test set. (b) The cumulative distribution function of all femur length measurements overlaid with the equivalent distribution for a fitted model using a mixed Gaussian + uniform distribution.

in a single frame. This appears to be random error: there is little observed bias.

Part of this difference can be explained by failure modes of our networks. Figure 7 shows some frames for which the

models give an inaccurate biometric estimate. This typically occurs when structures of interest are poorly visualised in the US image, or in some edge cases such as when both femurs are visible in a frame. These failure modes are uncommon (divergences of over 20% as shown in Figure 7 are seen in only 1.5% of segmentations) but they are not mistakes that a human is likely to make.

There is significant variation in human-machine difference across biometrics. TCD shows a very large MSD of over 10%, while other biometrics are significantly more closely aligned to the human measurement. Human inter-observer variability in TCD measurements has been reported as being between 3-5% [17], so the machine method appears to show significantly greater variability.

B. Whole-scan biometric estimation

The clinical standard for biometric measurement in fetal US relies on operator selection and annotation of a small number of individual frames. We take a different approach:

we analyse every frame in which the biometry is visible, and use all available measurements to generate a global estimate of the biometric. This avoids operator dependence associated with selection of standard planes, which can be a substantial contributor to inter-rater variability. Furthermore, it reduces the impact of random error from caliper placement in any one plane, which is also a significant source of variability.

The overall estimates of biometrics across a scan show better agreement with manual measurements than those from a single image. For instance, the TCD estimates across a scan show an average MSD with the manual measurement of 4.37%, compared to 10.1% for individual frames. This is despite the fact that the frames selected by the sonographers were removed: aggregating measurements from a diverse and unselected range of views of the anatomy results in a similar level of agreement with the sonographer. This value is also comparable with human inter-observer variability estimates found in the literature [17].

There are also few extreme outliers, demonstrating that our system achieves human-level performance. This is despite the fact that performance of our CNNs on individual frames is lower than that achieved by humans: our whole-scan estimation method can compensate for the errors introduced by our single-frame estimation CNNs. We expect that our whole-scan algorithm could therefore achieve superhuman performance in biometric estimation if the single-frame estimator can be improved to human level. The test-retest experiment we performed in Section IV-C provides support for this, showing the variability in biometric estimates across scans is much lower than that between humans.

Furthermore, our method allows us to estimate credible intervals in which a given biometric can be expected to lie. This is based on the distribution of measurements and the number of observations, as described in Section II-E. On average, this is smaller than the MSD by a factor of 1.4. However, the manual measurement itself displays variability α : assuming Gaussianity, MSD should be larger than the standard error by a factor of $\sqrt{2} \approx 1.4$. Therefore, the calculated standard error is in line with the observed variability in our estimates. Our credible intervals therefore provide a quantitative measure of the uncertainty in biometric estimation.

The system discussed in this paper treats single-frame measurements in a US scan as following a Gaussian distribution (when they are not due to misclassifications). Section IV-D shows that this is globally an appropriate assumption, with measurements following the expected distribution. The distribution of measurements within each scan may be variable, depending on the operator’s choice of scanning planes, but the Bayesian estimation method ensures that an optimal estimate is always achieved given the available data.

Another advantage of this system, when applied in real time, is that it requires no sonographer interaction to obtain biometrics. Much of a prenatal US scan is spent acquiring biometrics, and removing the need for this measurement can reduce scan time by up to a third [13]. A prospective trial of this system would be needed to estimate and quantify a time saving.

C. Whole-scan performance and test-retest reliability

Section IV-C shows results of our models on paired data from the same scan. Despite a small number of pairs, across all biometrics our models are more repeatable and consistent than humans. The standard deviation of the difference between measurements of the same subject was approximately half of that between human sonographers. Much of the remaining difference can likely be explained by the different views of the relevant biometrics acquired in each scan determined by sonographer technique and fetal lie. This experiment was conducted in a sample scanned with a different US scanner and at a higher gestational age range than the training dataset, yet the model outputs remained robust to this domain shift.

VI. CONCLUSION

This paper has demonstrated a novel method using machine learning to estimate fetal biometrics at the 20-week scan. The proposed method does not rely on measurements performed on individual manually-selected standard planes, as is the norm in both manual measurements and for many commercial machine assisted systems, but estimates biometrics across the entire scan. This avoids the biases exhibited by humans in plane selection and biometric measurement. We further present evidence that estimates produced using the proposed methods may be more consistent and repeatable than human measurements. This approach can also present other benefits that have not been quantified in this paper: by removing the need for sonographers to freeze the US stream and perform measurements, the system can improve sonographer focus and reduce the time needed to complete a FASP scan. A prospective trial of this system is in progress to establish whether this can realise those benefits and improve detection of fetal abnormalities.

DATA AVAILABILITY STATEMENT

The US scan recordings used to train the CNNs used in this paper were collected with an ethical requirement for patient data to remain confidential. As such, the scan data cannot be made publicly available. The raw and processed CNN outputs used to construct our results are available from the corresponding author on reasonable request.

ACKNOWLEDGEMENTS

This work was supported by the Wellcome Trust/EPSRC iFIND grant (IEH award 102431), by core funding from the Wellcome/EPSRC Centre for Medical Engineering [WT203148/Z/16/Z] and by the National Institute for Health Research (NIHR) Clinical Research Facility based at Guy’s and St Thomas’ NHS Foundation Trust and King’s College London.

COMPETING INTERESTS

The authors declare the following competing interests:

All authors are co-inventors on a patent filing related to the core methods described in this work filed by King’s College London (patent application number P333GB).

All authors are co-founders and hold equity ownership in Fraiya Ltd, an entity that is commercialising this technology.

REFERENCES

- [1] L. J. Salomon, Z. Alfirevic, F. D. S. Costa, R. L. Deter, F. Figueras, T. Ghi, P. Glanc, A. Khalil, W. Lee, R. Napolitano, A. Papageorgiou, A. Sotiradis, J. Stirnemann, A. Toi, and G. Yeo, "Isuog practice guidelines: ultrasound assessment of fetal biometry and growth," *Ultrasound in Obstetrics and Gynecology*, vol. 53, pp. 715–723, 6 2019.
- [2] N. H. S. England, "Fetal anomaly screening programme handbook," 2021.
- [3] L. J. Salomon, Z. Alfirevic, V. Berghella, C. M. Bilardo, G. E. Chalouhi, F. D. S. Costa, E. Hernandez-Andrade, G. Malinger, H. Munoz, D. Paladini, F. Prefumo, A. Sotiriadis, A. Toi, and W. Lee, "Isuog practice guidelines (updated): performance of the routine mid-trimester fetal ultrasound scan," *Ultrasound in Obstetrics and Gynecology*, vol. 59, pp. 840–856, 6 2022.
- [4] L. Drukker, R. Droste, P. Chatelain, J. A. Noble, and A. T. Papageorgiou, "Expected-value bias in routine third-trimester growth scans," *Ultrasound in Obstetrics and Gynecology*, vol. 55, pp. 375–382, 3 2020.
- [5] I. Sarris, C. Ioannou, P. Chamberlain, E. Ohuma, F. Roseman, L. Hoch, D. G. Altman, and A. T. Papageorgiou, "Intra- and interobserver variability in fetal ultrasound measurements," *Ultrasound in Obstetrics and Gynecology*, vol. 39, pp. 266–273, 2012.
- [6] C. F. Baumgartner, K. Kamnitsas, J. Matthew, T. P. Fletcher, S. Smith, L. M. Koch, B. Kainz, and D. Rueckert, "Sononet: Real-time detection and localisation of fetal standard scan planes in freehand ultrasound," *IEEE Transactions on Medical Imaging*, vol. 36, 2017.
- [7] H. Chen, Q. Dou, D. Ni, J. Z. Cheng, J. Qin, S. Li, and P. A. Heng, "Automatic fetal ultrasound standard plane detection using knowledge transferred recurrent neural networks," *Lecture Notes in Computer Science (including subseries Lecture Notes in Artificial Intelligence and Lecture Notes in Bioinformatics)*, vol. 9349, pp. 507–514, 2015.
- [8] X. P. Burgos-Artizzu, D. Coronado-Gutierrez, B. Valenzuela-Alcaraz, E. Bonet-Carne, E. Eixarch, F. Crispi, and E. Gratacos, "Evaluation of deep convolutional neural networks for automatic classification of common maternal fetal ultrasound planes," *Scientific Reports 2020 10:1*, vol. 10, pp. 1–12, 6 2020.
- [9] M. Sinclair, C. F. Baumgartner, J. Matthew, W. Bai, J. C. Martinez, Y. Li, S. Smith, C. L. Knight, B. Kainz, J. Hajnal, A. P. King, and D. Rueckert, "Human-level performance on automatic head biometrics in fetal ultrasound using fully convolutional neural networks," *Proceedings of the Annual International Conference of the IEEE Engineering in Medicine and Biology Society, EMBS*, vol. 2018-July, pp. 714–717, 10 2018.
- [10] M. Yaqub, N. Sleep, S. Syme, Z. Chen, H. Ryou, S. Walton, J. A. Noble, and A. T. Papageorgiou, "491 scannav Å® audit: an ai-powered screening assistant for fetal anatomical ultrasound," *American Journal of Obstetrics and Gynecology*, vol. 224, p. S312, 2 2021.
- [11] S. Plotka, T. Włodarczyk, A. Klasa, M. Lipa, A. Sitek, and T. Trzcinski, "Fetalnet: Multi-task deep learning framework for fetal ultrasound biometric measurements," *Communications in Computer and Information Science*, vol. 1517 CCIS, pp. 257–265, 2021.
- [12] C. Lee, A. Willis, C. Chen, M. Sieniek, A. Watters, B. Stetson, A. Uddin, J. Wong, R. Pilgrim, K. Chou, D. Tse, S. Shetty, and R. G. Gomes, "Development of a machine learning model for sonographic assessment of gestational age," *JAMA Network Open*, vol. 6, pp. e2248685–e2248685, 1 2023.
- [13] J. Matthew, E. Skelton, T. G. Day, V. A. Zimmer, A. Gomez, G. Wheeler, N. Toussaint, T. Liu, S. Budd, K. Lloyd, R. Wright, S. Deng, N. Ghavami, M. Sinclair, Q. Meng, B. Kainz, J. A. Schnabel, D. Rueckert, R. Razavi, J. Simpson, and J. Hajnal, "Exploring a new paradigm for the fetal anomaly ultrasound scan: Artificial intelligence in real time," *Prenatal Diagnosis*, vol. 42, pp. 49–59, 1 2022.
- [14] R. Smith, "An overview of the tesseract ocr engine," *Proceedings of the International Conference on Document Analysis and Recognition, ICDAR*, vol. 2, pp. 629–633, 2007.
- [15] *Voluson E8/E8 Expert Basic User Manual*. GE Healthcare, 2012.
- [16] B. 3rd Trimester Special Interest Group, "Professional guidance for fetal growth scans performed after 23 weeks of gestation," 2022.
- [17] M. R. Chavez, C. V. Ananth, J. C. Smulian, S. Lashley, E. V. Kontopoulos, and A. M. Vintzileos, "Fetal transcerebellar diameter nomogram in singleton gestations with special emphasis in the third trimester: A comparison with previously published nomograms," *American Journal of Obstetrics and Gynecology*, vol. 189, pp. 1021–1025, 10 2003.
- [18] "Labelbox | data-centric ai platform for building intelligent applications."
- [19] S. Constantine, A. Kiermeier, and P. Anderson, "The normal fetal cephalic index in the second and third trimesters of pregnancy," *Ultrasound Quarterly*, vol. 36, pp. 255–262, 2020.

APPENDIX A CNN FOR CALIPER LOCALISATION

A. Introduction



Figure 12. Zoomed examples of two calipers in the training set. These are at different scales, with different backgrounds and levels of overlap with other labels: it is difficult to design a machine method that can extract both reliably.

For this project, we used the sonographer’s annotations taken during their ultrasound scans as a source of data labels. These are readily visible in the scan and trivial for a human to detect: the calipers places by sonographers are prominent in their shape and colour. However, there were too many calipers to feasibly extract manually: approximately 40,000 labelled images were used in this paper.

Similarly, it is difficult to use a machine algorithm to extract these calipers automatically. Though all ultrasound scans were performed on identical hardware, there were several software updates over the course of the iFIND study, which changed the resolution and rendering of calipers. These weren’t always consistently rendered on the machine, as they appeared to be interpolated and therefore displayed differently. Furthermore, calipers often overlap with text annotations or other calipers, making it difficult to reliably distinguish them. Figure 12 shows two very different caliper shapes on different backgrounds.

We used a simple ML tool, which we called CaliperNet, to extract these labels automatically.

B. Labels and training

We used a sample of 300 images per standard plane to be manually annotated with caliper locations. We obtained these labels from a single human annotator on Labelbox [18]. Caliper locations are exact, so we expect very little labelling noise.

Labelbox does not have a native ellipse annotation facility, so to trace ellipse labels we asked the annotator to pinpoint five points along the perimeter of the ellipse: five points are sufficient to fully constrain an ellipse’s parameters. Training labels were generated in the same way as in the main paper: for length biometrics, the endpoints were convolved with a Gaussian kernel to generate a heatmap. For ellipse biometrics, the outline of the ellipse was convolved with a Gaussian kernel.

We used the same U-Net architecture as for our full biometric models to train CaliperNet. The only difference was

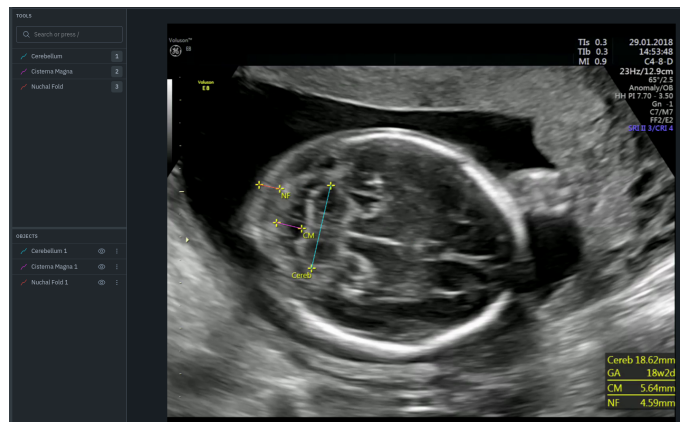


Figure 13. The interface of Labelbox which we used to annotate calipers, with an example annotation of a transcerebellar image with three manual annotations.

the retention of image colour channels: calipers in the GE interface are coloured yellow, while the rest of an ultrasound image is usually in greyscale (though the operator can change the colour map), so important information is carried by the colour channel.

We trained three separate models: one to extract ellipse annotations (such as HC and AC), one to extract caliper locations in the femur image, and one to extract TCD locations in transcerebellar brain images. The TCD model had to be trained separately as for most images in that plane, the sonographer took three annotations and placed three sets of calipers: the TCD, the cisterna magna (CM), and the nuchal fold (NF)⁸. Figure 13 shows an example image with three sets of calipers. For TCD calipers, we generated multi-channel labels, with one channel per annotated structure. Not all images in this standard plane had all three biometrics labelled: if calipers were missing, the relevant channel was left blank.

Training was performed using a 75:10:15 train:validation:test split for images. We used the same hardware to train CaliperNet models as the models described in the main paper.

C. Results

Biometric	Bias (%)	MSE (%)	Dice coefficient
HC	-0.01%	0.30%	0.821
AC	0.00%	0.34%	0.819
FL	+0.09%	0.66%	0.861
TCD	+0.07%	0.95%	0.946

Table VII
RESULTS FOR EACH CALIPERNET TRAINED ON ONE BIOMETRIC.

Table VII shows the performance of CaliperNet on our test dataset across the structures of interest. There is very little

⁸Of these, the TCD measurement is in the FASP standard and is required to always be measured. Nuchal fold must be measured only if it is abnormally thick, while cisterna magna was in a previous version of the FASP standard but is no longer required.



Figure 14. Annotations with the largest % errors in the test sets: green is the ground-truth annotation and pink are the CaliperNet outputs. Shown in (a) femur (length error of about 1%), and (b) abdomen (about 2%).

error, showing that this is a fairly straightforward task for these networks. Often, the pixel localisations are exactly the same: the errors are usually on the order of ± 1 px in specific pixel locations. The ‘Dice coefficient’ column measures how well the network output maps replicate the training labels. While it is high, it is not perfect: this may be because the limited training data makes it difficult for the CNN to learn to replicate the Gaussian kernels consistently. Nevertheless, the regressed endpoints and ellipses remain reliable.

There were no failure cases across our test dataset. Figure 14 shows the images with the largest errors (-1% and +2%) in biometric between the manual annotation of the calipers and the CaliperNet output. In both cases, the difference was of 1px in endpoint localisation - within labelling noise. This reflects the fact that caliper localisation is a trivial task for humans, and is not a challenging task for CNNs. Therefore, we can have confidence in the labels generated by CaliperNet and can use them to generate training labels for our biometric CNNs.

APPENDIX B

ADDITIONAL PERFORMANCE METRICS FOR BIOMETRIC CNNs

A. Introduction

Two additional metrics were used to measure the performance of our biometric CNNs and to filter for failure cases at test time. These could give substantial indicators of failure cases, making them useful to reject failure cases and reduce noise in our whole-video estimates. One metric, the Dice similarity coefficient of a reconstructed heatmap, was used to measure the quality of fit of derived ellipses and points from the CNN’s heatmap: where this was too low, the fit was deemed of insufficient quality to accept the resulting measurement. The other was the eccentricity of the output ellipses for head and abdominal circumference measurements: where this was anatomically implausible, the measurements were rejected.

B. Dice similarity coefficient

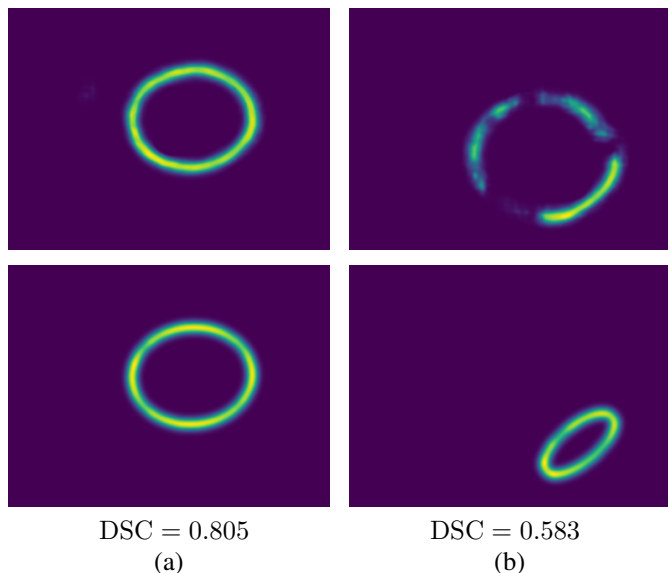


Figure 15. Two comparisons of the output heatmap from a CNN and the resulting ‘reconstructed’ ellipse. (a) a success case with $DSC = 0.805$, (b) a failure case with $DSC = 0.583$.

The Dice similarity coefficient (DSC) is a measure of overlap between two sets defined as

$$DSC(X, Y) = \frac{2|X \cap Y|}{|X| + |Y|}$$

and is often used in image segmentation tasks to measure how closely a segmentation follows the ground truth.

Our biometric CNNs output heatmaps based on endpoints and ellipses, as described in Section II-D. These are then processed to return a biometric measurement: for linear measurements, endpoints are found from local maxima of the heatmap; for ellipses, an ellipse is fit using least-squares to the heatmap.

This can then be checked by generating a heatmap from the resulting annotation, using the same process described in Section II-D. The two heatmaps should match exactly in

the case of a perfect output. In reality, there is always some deviation, but when the reconstructed ellipse faithfully follows the output heatmap, the resulting DSC is high.

We found that a $DSC < 0.6$ between the output heatmap and the reconstruction indicated a poor reconstruction of the CNN output. Therefore, we discarded any proposed reconstructions that fell below that threshold, as the output would be very noisy and inaccurate in following anatomical boundaries.

Figure 15 shows two example cases of reconstructed ellipses based on an output heatmap. (a) shows a success case, where the reconstructed ellipse closely follows the output heatmap: this would be accepted. (b) shows a case where the output heatmap is quite noisy and results in poor fit of the reconstructed ellipse. This has low DSC and therefore is rejected.

C. Ellipse eccentricity

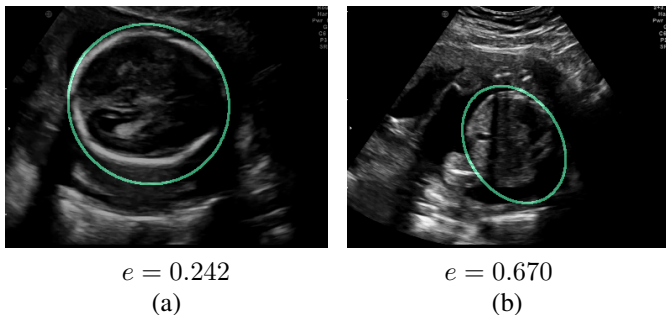


Figure 16. Biometric failure cases which violate the eccentricity constraint in (a) the head, and (b) the abdomen.

For ellipse biometrics (HC and AC), another relevant metric to consider at test time is eccentricity.

$$e = \sqrt{1 - \frac{a^2}{b^2}}$$

where a is the minor axis of the ellipse and b is the major axis. For the head, a is the BPD measure and b is the OFD (occipito-frontal diameter). While this is a commonly used mathematical measure, in obstetrics the more common measure for head measurements is the **cephalic index**, defined as

$$CI = \frac{a}{b} \times 100.$$

In the case of an ellipse, there is a 1:1 correspondence between the two measures, where

$$e = \sqrt{1 - \left(\frac{CI}{100}\right)^2}.$$

In the 17-22 week range of gestational age, the mean cephalic index has been reported as 75.9, with a standard deviation of 3.7 [19]. Therefore, an anatomically plausible range of cephalic indices is 65 – 90, which corresponds to an eccentricity range of 0.43 – 0.76. Any ellipse with an eccentricity outside of this range is likely to be a failure mode of the biometric CNN.

In the final product using this CNN, we relaxed this constraint further to an eccentricity range of 0.25 – 0.8. This was

to restrict rejections to clear failures, allowing a large margin for biological variation.

The fetal abdomen has somewhat different morphology. It is typically round, with a very low eccentricity. We constrained it to have $e < 0.6$ for the purposes of our software - any abdominal ellipse with a higher eccentricity was considered biologically implausible and rejected.

Figure 16 shows two examples of drawn ellipses which violate this eccentricity constraint. Both are clear failures, where the ellipse does not follow anatomical boundaries. The addition of our constraint rejects the measurements from these ellipses as noise, even if the circumferences appear biologically plausible.

D. Plane classification confidence

Standard plane	Frames >95% confidence (%)
Brain-TV	83.5%
Brain-CB	82.1%
Abdominal	73.2%
Femur	66.4%

Table VIII
PROPORTION OF FRAMES IN THE FOUR BIOMETRIC STANDARD PLANES WHICH ARE CLASSIFIED WITH >95% SOFTMAX CONFIDENCE.

Section II-E describes one filtering method: only frames identified with $> 95\%$ confidence as a standard plane with a FASP biometric are processed by biometric networks. This somewhat reduces the number of frames passed to biometric networks and therefore the number of samples of each biometric.

Table VIII shows the proportion of frames classified as belonging to each of the four biometric standard planes with sufficient confidence for a measurement. In all cases, only a minority of frames are discarded.